Phys Chem Minerals (2002) 29: 319–330
DOI 10.1007/s00269-002-0240-z

ORIGINAL PAPER

U. Hålenius · H. Skogby · G.B. Andreozzi

Influence of cation distribution on the optical absorption spectra of Fe^{3+}-bearing spinel *s.s.*–hercynite crystals: evidence for electron transitions in $^{VI}Fe^{2+}$–$^{VI}Fe^{3+}$ clusters

Received: 30 August 2001 / Accepted: 18 December 2001

Abstract Flux-grown Fe^{3+}-bearing spinel *s.s.*–hercynite solid-solution crystals, $(Mg_{1-y}Fe^{2+}_y)Al_2O_4$ $(0 < y \leq 1)$, have been investigated by means of electron microprobe technique and Mössbauer and electronic spectroscopy. Obtained results show that different electronic processes cause intense optical absorption bands in the near-infrared spectral region. In addition to an electronic *d–d* transition in single-ion $^{IV}Fe^{2+}$, observed at 5200 cm^{-1}, intense and broad bands at 9500 and 14 500 cm^{-1} are assigned to exchange-coupled pair (ECP) and intervalence charge-transfer (IVCT) transitions in $^{VI}Fe^{2+}$ $^{VI}Fe^{3+}$clusters, respectively. The net linear extinction coefficients of these bands (α) were calibrated against Fe^{2+} and Fe^{3+} concentrations and site distributions previously defined by combined microchemical, Mössbauer, and XRD structural refinement data. The following expressions were obtained:

$$\alpha_{5200} = 59 \pm 4\ [^{IV}Fe^{2+}],\ \alpha_{9500} = 189 \pm 36\ [^{VI}Fe^{2+}][^{VI}Fe^{3+}]$$
$$\text{and}\quad \alpha_{14500} = 141 \pm 25\ [^{VI}Fe^{2+}][^{VI}Fe^{3+}]\ ,$$

where α is measured in cm^{-1} and concentrations are expressed in mol l^{-1}.

The present results show that optical absorption spectroscopy may be used as a probe to obtain high spatial resolution ($\varnothing \sim 10$ μm) information on Fe^{2+} ordering as well as on Fe^{3+} concentrations in minerals belonging to the spinel group.

Keywords Spinel · Hercynite · Cation ordering · Mössbauer spectroscopy · Electronic spectroscopy

U. Hålenius (✉) · H. Skogby
Department of Mineralogy,
Swedish Museum of Natural History,
Box 50007, 104 05 Stockholm, Sweden
e-mail: ulf.halenius@nrm.se

G. B. Andreozzi
Dipartimento di Scienze della Terra, Universita' di Roma
La Sapienza, P.le A. Moro 5, 00185, Roma, Italy

Introduction

Spinel-bearing mineral associations are almost ubiquitous in most geological environments of the lower crust and upper mantle, as well as in extraterrestrial materials. The Fe^{2+}–Fe^{3+} spinels (e.g., magnetite) are important indicators of oxygen fugacity in the host rocks, and they contribute to the crustal magnetism (Haggerty 1978; Frost and Shive 1986; O'Neill and Wall 1987; Mattioli and Wood 1988). The nonmagnetic spinels (e.g., Fe^{2+}–Mg aluminate) are more important as indicators of temperature and/or pressure, due to both temperature-dependent intracrystalline cation ordering and equilibria with associated Fe–Mg silicates (Della Giusta et al. 1996; Lucchesi and Della Giusta 1997; Lucchesi et al. 1998a; Princivalle et al. 1999).

The spinel structure is made up by a cubic close-packing oxygen array with cations filling in 1/8 of the tetrahedral (T) and 1/2 of the octahedral (M) cavities. In the ideal cubic structure, when origin is set at the center of symmetry ($\bar{3}m$), the single oxygen atom is at (1/4 1/4 1/4) fractional coordinates, and the occupied T site ($\bar{4}3m$) and M site ($\bar{3}m$) are at (1/8 1/8 1/8) and (1/2 1/2 1/2), respectively. Real spinel structures are best described by a slightly distorted cubic array with free (u u u) oxygen fractional coordinates. Every variation of u, i.e., of oxygen position along the [1 1 1] direction, determines modifications of T–O and M–O bond distances, and allows for accommodation of various chemical components and/or cation ordering. Real spinels usually have u parameters higher than the ideal value 0.25, and this corresponds to larger tetrahedral sites at the expense of decreased octahedral sites, still with fixed coordinates (Hafner 1960; Hill et al. 1979).

In the spinel structural framework, octahedral sites share half of their polyhedral edges, octahedral and tetrahedral sites share polyhedral corners, but tetrahedra show no mutual ligands (Fig. 1). In effect, every tetrahedron is surrounded by 12 octahedra, whereas every

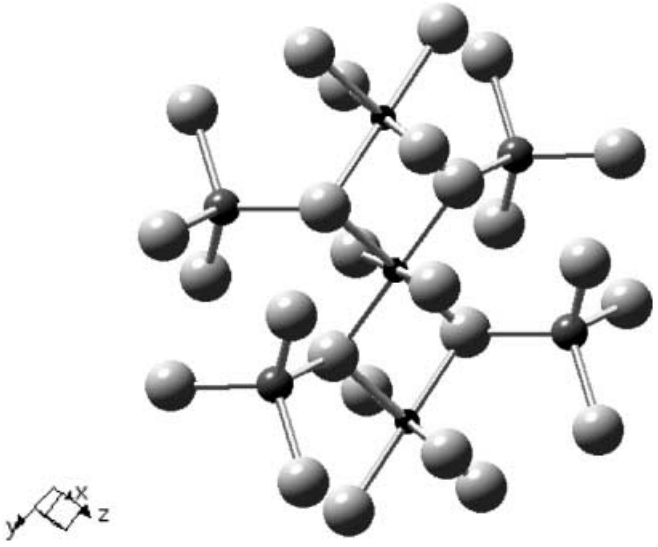

Fig. 1 The spinel structure plotted approximately along [2 0 $\bar{1}$]. *Small*, *black spheres* M cations; *intermediate*, *gray spheres* T cations; *large*, *light gray spheres* oxygen anions

octahedron is surrounded by six octahedra and six tetrahedra. In view of this closely packed array of octahedral and tetrahedral sites, the spinel structure must be considered a very strong candidate for electronic IVCT and ECP processes. In fact, $^{IV}Fe^{3+}$–$^{VI}Fe^{3+}$ ECP absorption was recently demonstrated in the optical spectra of spinel *s.s.*–magnesioferrite solid-solution crystals (Andreozzi et al. 2001b). In the present work we are exploring effects of cation distribution in the system spinel *s.s.*–hercynite, with the aim to detect additional optically active clusters among common spinel-group minerals and evaluate their potential use for analysis of cation order.

Previous studies

Cation distribution in spinels might be described by the $^{IV}(A_{1-i}B_i)^{VI}(B_{2-i}A_i)O_4$ structural formula, where IV and VI represent the tetrahedrally and octahedrally coordinated T and M sites, respectively. A and B are cations with different valences, and i represents the inversion parameter. At low temperature, i tends to 0 in normal spinels (e.g., spinel *s.s.* $MgAl_2O_4$, hercynite $FeAl_2O_4$) and to 1 in inverse spinels (e.g., magnesioferrite $MgFe_2O_4$, magnetite $FeFe_2O_4$), whereas at elevated temperature i values are shown to converge asymptotically toward 2/3 for all compositions (O'Neill et al. 1992; O'Neill and Dollase 1994; Harrison et al. 1998; Redfern et al. 1999; Andreozzi et al. 2000). Both normal and inverse configurations are ordered, whereas $i = 2/3$ corresponds to maximum disorder, i.e., each site displays the same occupancy. Cation disordering does not induce modifications of the cubic *Fd3m* symmetry, and hence the process is nonconvergent.

Continuous solid solution has been experimentally observed at temperatures below 1000 °C between spinel *s.s.* and hercynite, whereas the existence of a large immiscibility gap between hercynite and Mg–Fe ferrites has been demonstrated (Turnock and Eugster 1962; Lehmann and Roux 1986). At each $T > 0$ K, a fraction of the Fe^{2+} is inverted for all members of solid solutions containing hercynite, i.e., ferrous iron is partly present as $^{VI}Fe^{2+}$. Whether this fraction is constant at a given temperature, i.e., is compositionally independent, is still unknown. From the work of Larsson (1994, 1995) and Larsson et al. (1994), a constant fraction of $^{VI}Fe^{2+}$ with respect to total Fe^{2+} is suggested along the spinel *s.s.*–hercynite join. In contrast, Waerenborgh et al. (1994) demonstrated an increasing fraction of $^{VI}Fe^{2+}$ with respect to total Fe^{2+} for samples along the gahnite–hercynite join.

In previous optical absorption studies of Fe-bearing spinel-group minerals, an intense band at 4500–5000 cm^{-1} was assigned to a spin-allowed electronic *d–d* transition ($^5E \rightarrow {}^5T_2$) in tetrahedrally coordinated ferrous iron (e.g., Slack et al. 1966; Gaffney 1973; Mao and Bell 1975; Dickson and Smith 1976). Spectra of spinel minerals extending into the IR range reveal additional absorption bands down to approximately 3600 cm^{-1}, which have been explained in terms of dynamic Jahn–Teller effects as well as phonon-coupling (Slack et al. 1966; Taran and Langer 2001; Rossman and Taran 2001). Moreover, a number of very weak spin-forbidden *d–d* bands in the region 11 000–18 000 cm^{-1} have been observed (e.g., Gaffney 1973). Only one absorption band caused by a spin-allowed transition ($^5T_{2g} \rightarrow {}^5E_g$) in octahedrally coordinated ferrous iron has been recorded at ~10 000 cm^{-1} in spinel spectra (Mao and Bell 1975; Dickson and Smith 1976). In relation to the $^{IV}Fe^{2+}$ band at ~5000 cm^{-1}, this $^{VI}Fe^{2+}$ band is considerably weaker as a consequence of the Fe^{2+} order in spinel as well as of differences in molar extinction coefficient (ε) for the two bands. The lower ε value may be ascribed to the centrosymmetric character of the octahedral M site.

In addition to single-ion electronic transitions, a number of different processes are known to cause prominent absorption bands in VIS/NIR spectra of oxygen-based minerals containing transition metal cations of different charge (e.g., Burns 1993). The most important cooperative processes are electron charge transfers (IVCT) between neighboring heterovalent cations in edge- or face-sharing coordination sites (e.g., Mattson and Rossman 1987a) and exchange-coupled pair transitions (ECP) involving cations at neighboring structural sites (e.g., Smith 1978; Mattson and Rossman 1987b). Absorption bands due to exchange-coupled Fe^{2+}–Fe^{3+} pairs generally occur close to or at the energies of the single-ion *d–d* transitions of the pair cations, and the extinction coefficients of the bands are strongly enhanced with respect to bands caused by single-ion *d–d* transitions (e.g., Smith 1978). In contrast, Fe^{2+}–Fe^{3+} IVCT bands generally display higher ener-

gies, typically in the range 12 000–17 000 cm^{-1}, than those recorded for spin-allowed single-ion *d–d* bands due to ferrous iron at regular octahedral or tetrahedral sites (Mattson and Rossman 1987a). Bands of IVCT origin show molar extinction coefficient orders of magnitudes higher than normal single-ion *d–d* bands (e.g., Burns 1993). Furthermore, the net extinction coefficients of ECP as well as of IVCT bands are considered to be directly correlated with the concentration product of the interacting cations (e.g., Smith 1978).

Experimental

Crystal synthesis

Single crystals along the spinel *s.s.*–hercynite join were synthesized using a flux-growth method. Analytical grade $Al(OH)_3$, MgO, and Fe_2O_3 powders were dehydrated and dried at 1000 °C for 12 h before mixing with $Na_2B_4O_7$, used as flux compound. About 5 g of starting material was thoroughly ground under acetone in an agate mortar and mixed, with flux/nutrients ratios ranging from 1.3 to 1.4. A 10-cc crucible of yttria-stabilized Pt/Au (5%) was chosen as reaction vessel due to its high resistance to chemicals at high temperatures in reducing conditions (Okaj et al. 1996). Thermal runs were performed in a vertical furnace equipped with Tylan CO_2:H_2 flow controllers. Continuous flow of the two gases at constant ratios (Table 1) was adopted to obtain oxygen fugacity ranging from 10^{-11} to 10^{-17} bar when temperature was varied from 1200 to 900 °C. These fO_2 values are within −0.3 to +1.2 log units relative to the iron/wüstite solid buffer. In order to obtain a homogeneous melt, the load was heated for 24 h at 1200 °C, and subsequently the temperature was decreased applying slow cooling (2–4 °C h^{-1}). Turning off the furnace ended thermal runs and the product was allowed to cool to room temperature. Products consisted of spinel single crystals and in some runs also borate crystals embedded in sodium borate glass. The glass was dissolved in warm, dilute HCl solution, reducing final products to euhedral or subhedral octahedra of spinel (ranging 0.1–1.0 mm across) with occasional lath-shaped borate crystals. Up to 200 mg of high-quality spinel crystals of about 0.2–0.5 mm were recovered from each experiment. Some of these crystals were selected for structure refinement through single-crystal XRD (Andreozzi and Lucchesi 2002) and some others for optical absorption spectroscopy (OAS). Most of the remaining material was powdered and used for Mössbauer spectroscopy (MS).

Chemical and spectral analysis

The crystals used for optical absorption spectroscopy were mounted on glass slides, polished and carbon-coated for electron microprobe analysis, WDS method, on a Cameca-Camebax instrument operating at an acceleration voltage of 15 kV and a sample current of 15 nA. Synthetic MgO, Fe_2O_3, Al_2O_3 standards were used, and a synthetic $MgAl_2O_4$ sample was used as reference material. For raw data reduction, the PAP computer program was applied (Pouchou and Pichoir 1984). Each element determination was accepted after checking that measurements of standards before and after sample determination were within ±1%. A minimum of 6 to a maximum of 25 microanalyses was performed on each sample in the same area as that studied by OAS. Sodium was checked as possible contaminant but was not detected in any sample. The absence of boron in spinels synthesized using the same experimental conditions was confirmed by means of $^{11}B(p,2\alpha)^4He$ nuclear reaction analysis (Kristiansson et al. 1999). Contents of FeO and Fe_2O_3 were calculated on the basis of stoichiometry requirements (three cations per four oxygens) and turned out to be in reasonable agreement with MS data collected on the same material.

^{57}Fe Mössbauer spectra were obtained for all samples except the one with the lowest hercynite component (He2d). Absorbers were prepared by pressing finely ground samples with a powdered acrylic resin (transoptic powder) to self-supporting discs with an Fe thickness of 1–2 mg cm^{-2}. Spectra were collected at both room and liquid-nitrogen temperatures using a conventional spectrometer system operated in constant acceleration mode with a ^{57}Co source in rhodium matrix. Low-temperature spectra were collected, as a consequence of the cryostat design, with the absorber at an angle of 54.7° to the incident beam, and consequently the effective thickness increased by a factor of 1.7. Spectral data for the velocity range −4.5 to 4.5 mm s^{-1} were recorded in a multichannel analyzer using 1024 channels. After velocity calibration by aid of spectra of α-iron foil, the raw data in the 1024 channels were reduced to 512 and then folded to 256 channels. The spectra were fitted in this format using a least-squares fitting program (Jernberg and Sundqvist 1983) and assuming Lorentzian peak shapes.

Optical absorption spectra of the present synthetic samples were obtained at room temperature from double-sided polished single crystals. The absorber thickness was in the range 11–245 μm as determined by means of a digital micrometer. All spectra were recorded with a Zeiss MPM800 single-beam spectrometer using Zeiss Ultrafluar 10x lenses as objective and condenser. In the UV/VIS spectral range, a 75-W Xenon arc lamp served as a light source and a photomultiplier as detector. In the NIR spectral region (from 12 500 to ca. 4500 cm^{-1}), a 100-W halogen lamp was used as a light source and light detection was achieved by means of a photoconductive PbS cell. Spectra were recorded at a spectral resolution of

Table 1 Electron microprobe analysis of synthetic spinel crystals on the join spinel *s.s.*–hercynite. Average oxide weight percentages and standard deviations (1σ) of 6 to 25 analyses in the same area as that investigated by microscope optical absorption spectroscopy. FeO and Fe_2O_3 were recalculated on the basis of stoichiometry, three cations per four anions, and Fe^{3+}/Fe^{2+} ratios were confirmed by Mössbauer spectroscopy

Samples	He2d	He2f	He3a	He4b	He5a	He6a	He7a	He8a	He9a	He100c	$He100c_{rim}$	He100e	He100g
CO_2:H_2[a]	1:1	2:1	2:1	2:1	2:1	2:1	2:1	2:1	2:1	2:1	2:1	1:1	1:2
MgO	27.9(2)	26.9(2)	25.5(1)	19.4(1)	16.6(1)	13.7(1)	10.5(1)	7.0(1)	4.23(7)	–	–	–	–
FeO	1.05(9)	2.1(1)	4.7(2)	12.9(2)	17.2(1)	21.2(2)	25.8(2)	30.9(1)	34.5(4)	40.8(4)	41.0(3)	41.0(3)	41.1(3)
Fe_2O_3	0.15(9)	0.2(1)	0.8(2)	0.8(2)	1.0(1)	2.1(2)	2.6(2)	2.3(1)	3.7(4)	4.4(4)	3.4(3)	1.9(3)	1.2(3)
Al_2O_3	71.7(3)	71.1(3)	69.9(4)	67.3(2)	65.8(3)	63.3(2)	61.5(4)	60.0(2)	57.3(3)	55.1(2)	56.0(2)	57.0(4)	57.5(4)
Total	100.80	100.3	100.9	100.4	100.6	100.3	100.4	100.2	99.73	100.3	100.4	99.9	99.8
Number of cations on the basis of four oxygens													
Mg	0.980(6)	0.957(3)	0.911(3)	0.725(4)	0.632(2)	0.536(4)	0.421(4)	0.287(4)	0.179(3)	0.000	0.000	0.000	0.000
Fe^{2+}	0.021(2)	0.042(3)	0.094(4)	0.270(4)	0.367(2)	0.464(4)	0.579(5)	0.713(3)	0.821(8)	1.000(7)	1.000(6)	1.000(1)	1.000(1)
Fe^{3+}	0.003(2)	0.003(3)	0.015(4)	0.015(4)	0.019(2)	0.041(4)	0.052(5)	0.048(4)	0.079(7)	0.098(6)	0.075(4)	0.041(6)	0.027(6)
Al	1.996(4)	1.998(4)	1.980(5)	1.990(4)	1.982(3)	1.959(4)	1.948(6)	1.952(4)	1.921(8)	1.902(7)	1.925(6)	1.959(6)	1.973(6)
Total	3.000	3.000	3.000	3.000	3.000	3.000	3.000	3.000	3.000	3.000	3.000	3.000	3.000

[a] CO_2:H_2 gas-mixing ratio during synthesis

2.5 nm in the UV/VIS range and 5 nm in the NIR region, and the measure spot was 40 μm.

Recorded spectra were deconvoluted using the peak resolution program Jandel PeakFit 4.0. In the deconvolution process all fitted bands were assumed to be of Gaussian shape. The recorded UV-absorption edges were also fitted with a Gaussian function. No other constraints were applied during the fitting procedure.

Results

Spinel *s.s.*–hercynite crystal chemistry

The crystals obtained varied in color, depending on hercynite content, from colorless spinel *s.s.*, and with increasing total Fe content, to pale lilac, sky blue, green, and deep green. Crystals close to the hercynite end member appeared as black (Fig. 2).

The chemical composition is obviously dominated by the Fe^{2+}–Mg substitution: along the join with the Fe^{2+} content ranging from 0.02 to 1.00 atoms per formula unit (apfu) and the Mg content from 0.98 to zero apfu (Table 1). The Al content is not far from its stoichiometric value (2 apfu), although a very minor decrease may be observed from sample He2d to He100c. This apparent Al deficiency is compensated by the presence of Fe^{3+}, which increases from almost zero up to 0.10 apfu from sample He2d to He100c. Samples He100e and He100g, which were synthesized at more reducing conditions, show considerably lower Fe^{3+} contents. In particular, decreasing the oxygen fugacity of the gas mixture below the iron/wustite solid buffer and adding more Al to the nutrient mixture reduced the Fe^{3+} content, but this latter never became null. This could be due to an active role of the spinel structure in stabilizing Fe^{3} or an insufficient Al activity in the melt phase. Comparable deviations from the stoichiometry of hercynite due to anomalous Fe^{3+} contents have frequently been observed in both synthetic and natural spinel samples (Slack 1964; Cremer 1969; Hill 1984; Bohlen et al. 1986; Waerenborgh et al. 1994; Larsson et al. 1994; Della Giusta et al. 1996).

Structure refinement data of the present crystals (Andreozzi et al. 2001a, Andreozzi and Lucchesi 2002) show that the cell edge *a*, oxygen position *u*, and the bond distance T–O increase linearly with the hercynite content, whereas the M–O distance remains almost constant. The *a* variation (from 8.0855 to 8.1646 Å) is essentially caused by the T–O increase (from 1.920 to 1.968 Å), which, in turn, is due to the cooperative effects of chemical substitution $Fe^{2+} \rightarrow Mg$ and decrease of inversion (from 0.25 to 0.15) along the spinel *s.s.*–hercynite join. Site distributions of Mg and Al as well as Fe^{2+} and Fe^{3+} (Andreozzi and Lucchesi 2002) were obtained on site-scattering and bond-distance basis by combining structural and microchemical data by means of a minimization procedure that has provided excellent results in processing spinel data (Lucchesi et al. 1998a,b, 1999; Andreozzi et al. 2001c). These cation distributions (Table 2) are confirmed by the Mössbauer data presented here (Table 3). Both minimized and observed amounts of $^{VI}Fe^{2+}$ show a nonlinear increase from spinel *s.s.* to hercynite, i.e., with increasing total Fe^{2+}. Consequently, the $^{VI}Fe^{2+}/Fe^{2+}_{tot}$ ratio is not constant along the join, but increases from zero to 0.15 towards the hercynite end member.

Mössbauer spectroscopy

Both low- and room-temperature spectra are dominated by a broad absorption doublet that at liquid-nitrogen temperature has a mean quadrupole splitting between

Fig. 2 Microphotograph of selected spinel–hercynite solid-solution crystals illustrating color variations in response to hercynite concentration (increasing *to the right*)

Table 2 Crystal-chemical formula of synthetic crystals of the spinel *s.s.*–hercynite solid solution. (Andreozzi and Lucchesi 2002)

Sample	Inversion	Formula
He2f	0.24	$^{IV}(Mg_{0.715}Fe^{2+}_{0.046}Al_{0.239})^{VI}(Mg_{0.239}Al_{1.761})O_4$
He3a	0.25	$^{IV}(Mg_{0.640}Fe^{2+}_{0.111}Al_{0.249})^{VI}(Mg_{0.250}Al_{1.750})O_4$
He4b	0.22	$^{IV}(Mg_{0.514}Fe^{2+}_{0.272}Al_{0.214})^{VI}(Mg_{0.213}Fe^{2+}_{0.004}Al_{1.769}Fe^{3+}_{0.015})O_4$
He5a	0.22	$^{IV}(Mg_{0.434}Fe^{2+}_{0.347}Al_{0.219})^{VI}(Mg_{0.215}Fe^{2+}_{0.008}Al_{1.762}Fe^{3+}_{0.016})O_4$
He6a	0.21	$^{IV}(Mg_{0.366}Fe^{2+}_{0.424}Al_{0.194}Fe^{3+}_{0.016})^{VI}(Mg_{0.178}Fe^{2+}_{0.035}Al_{1.768}Fe^{3+}_{0.020})O_4$
He7a	0.20	$^{IV}(Mg_{0.267}Fe^{2+}_{0.531}Al_{0.192}Fe^{3+}_{0.010})^{VI}(Mg_{0.153}Fe^{2+}_{0.054}Al_{1.772}Fe^{3+}_{0.022})O_4$
He8a	0.19	$^{IV}(Mg_{0.185}Fe^{2+}_{0.630}Al_{0.168}Fe^{3+}_{0.017})^{VI}(Mg_{0.118}Fe^{2+}_{0.072}Al_{1.770}Fe^{3+}_{0.041})O_4$
He9a	0.18	$^{IV}(Mg_{0.101}Fe^{2+}_{0.713}Al_{0.152}Fe^{3+}_{0.034})^{VI}(Mg_{0.076}Fe^{2+}_{0.114}Al_{1.774}Fe^{3+}_{0.037})O_4$
He100c	0.15	$^{IV}(Fe^{2+}_{0.849}Al_{0.133}Fe^{3+}_{0.018})^{VI}(Fe^{2+}_{0.153}Al_{1.765}Fe^{3+}_{0.082})O_4$

2.5 and 3.0 mm s^{-1} (Fig. 3). In agreement with the literature on MS data interpretation, this part of the absorption envelope is considered to be due to ferrous iron. For the end-member hercynite samples, the broad doublet becomes partly resolved in an inner and an outer doublet. In accordance with previous studies (e.g., Larsson et al. 1994; Waerenborgh et al. 1994), the inner doublet is assigned to octahedrally coordinated Fe^{2+} and the broader outer doublet to tetrahedrally coordinated Fe^{2+}. A broad absorption for Fe^{2+} in the T site can be expected due to the variability of cation distributions in the second coordination sphere of this site (Waerenborgh et al. 1990). A weak band due to ferric iron is present in the spectra of samples with high hercynite components. For the low-hercynite compositions, this band is no longer resolved but contributes to the low-velocity half of the doublet, which has a larger absorption area than the high-velocity half. This indicates the presence of a ferric iron doublet also for these samples.

Several fitting strategies were tested to find a robust model that could be used throughout the solid solution with as few constraints as possible. The final model consisted of three outer doublets representing the broad $^{IV}Fe^{2+}$ contribution, one inner doublet for the $^{VI}Fe^{2+}$, and one weak doublet due to Fe^{3+} (Fig. 3). The hyperfine parameters thus obtained are listed in Table 3. The fitting model is similar to the one used by Waerenborgh et al. (1994) for a series of gahnite – hercynite samples, although they used a quadrupole splitting distribution for the $^{IV}Fe^{2+}$ absorption feature.

The intensity of the doublet assigned to $^{VI}Fe^{2+}$ increases with hercynite content and, as already mentioned, this is in agreement with structural refinement results (Table 2). It follows that $^{VI}Fe^{2+}/Fe^{2+}_{tot}$ is not constant along the solid solution but there is a compositional effect, and this is in line with previous observations (Waerenborgh et al. 1994; Andreozzi and Lucchesi 2002). Conversely, this is not in agreement with results of Larsson (1994, 1995) and Larsson et al. (1994), from which a linear increase of $^{VI}Fe^{2+}$ with increasing hercynite content (i.e., a constant $^{VI}Fe^{2+}/Fe^{2+}_{tot}$ ratio) may be inferred. However, the disagreement may be due to the low resolution of the $^{IV}Fe^{2+}$ and $^{VI}Fe^{2+}$ absorption bands in spinel Mössbauer spectra even at low temperature.

The peak position and width for the ferric iron doublet was initially fixed during the fitting procedure for the hercynite end-member samples with low Fe^{3+} contents (He100e and He100g). The obtained hyperfine parameters are in agreement with those observed for $^{VI}Fe^{3+}$ at low temperature in hercynite (Larsson et al. 1994; Waerenborgh et al. 1994) and magnesioferrite samples (H. Skogby 2000, unpublished).

Our results indicate that ferric iron increases from low-hercynite samples towards the sample He100c, although some scatter is evident. For the two samples

Table 3 Mössbauer parameters obtained for synthetic spinel-hercynite samples at 80 K. Hyperfine parameters are given in mm s^{-1}

Assignment	He2f	He3a	He4b	He5a	He6a	He7a	He8a	He9a	He100c	He100e	He100g
$^{IV}Fe^{2+}$ (1)											
int[a]	37.7	28.0	27.9	28.6	30.0	28.5	30.9	30.9	33.6	39.9	39.4
fwhm[b]	0.28	0.26	0.27	0.25	0.26	0.28	0.28	0.25	0.28	0.32	0.28
cs[c]	1.04	1.03	1.03	1.04	1.04	1.04	1.05	1.04	1.05	1.06	1.05
dq[d]	2.87	2.80	2.80	2.89	2.85	2.84	2.98	2.87	2.97	2.98	2.97
$^{IV}Fe^{2+}$ (2)											
int	26.2	26.8	25.1	24.4	22.9	23.0	24.1	21.8	22.3	19.5	20.5
fwhm	0.31	0.30	0.31	0.28	0.28	0.29	0.28	0.28	0.28	0.29	0.26
cs	1.04	1.03	1.03	1.04	1.04	1.04	1.05	1.05	1.06	1.05	1.05
dq	2.56	2.47	2.48	2.59	2.54	2.50	2.67	2.56	2.68	2.67	2.68
$^{IV}Fe^{2+}$ (3)											
int	25.3	30.6	30.9	28.4	26.7	28.7	24.7	26.6	21.2	21.8	21.6
fwhm	0.48	0.49	0.48	0.45	0.42	0.44	0.42	0.40	0.40	0.45	0.44
cs	1.03	1.04	1.03	1.05	1.04	1.03	1.06	1.04	1.07	1.07	1.08
dq	2.10	1.96	1.99	2.16	2.12	2.07	2.28	2.13	2.26	2.28	2.27
$^{VI}Fe^{2+}$											
int	8.5	10.3	12.4	14.9	15.3	15.3	14.7	14.9	16.5	16.4	17.4
fwhm	0.44	0.42	0.44	0.51	0.48	0.50	0.54	0.48	0.51	0.50	0.46
cs	1.02	1.02	1.03	1.05	1.05	1.04	1.09	1.07	1.10	1.13	1.13
dq	1.35	1.25	1.29	1.40	1.41	1.35	1.56	1.42	1.59	1.60	1.58
Fe^{3+}											
int	2.3	4.3	3.7	3.7	5.2	4.5	5.6	5.8	6.4	2.5	1.1
fwhm	0.38	0.30	0.30	0.41	0.42	0.43	0.42	0.41	0.37	0.42	0.40
cs	0.33	0.29	0.32	0.39	0.44	0.50	0.47	0.53	0.49	0.49	0.49
dq	0.40	0.72	0.81	0.80	0.79	0.66	0.87	0.76	0.91	0.86	0.90

[a] int = intensities given in % of total absorption area
[b] fwhm = full width at half maximum
[c] cs = centroid shift
[d] dq = quadrupole splitting

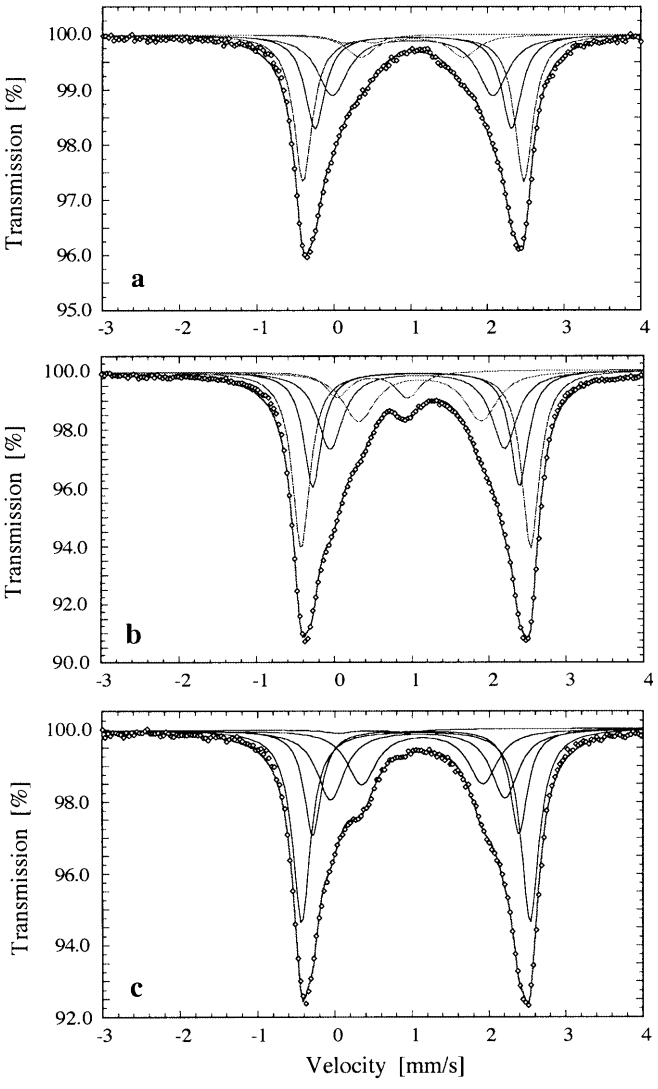

Fig. 3a–c Low-temperature Mössbauer spectra of some synthetic samples on the spinel *s.s.*–hercynite join. **a** Sample He2f. **b** Sample He100c. **c** Sample He100g

He100e and He100g, synthesized at considerably lower oxygen fugacities, MS data indicate a drastic decrease in the Fe^{3+}/Fe_{tot} ratio. Due to the low degree of resolution of the absorption doublets in the present spectra, the obtained hyperfine parameters have to be considered with some caution. However, the intensity data for ferric iron can be regarded as reliable, since the absorption area is either partly resolved or represented as an asymmetry in the spectra.

Optical absorption spectroscopy

Recorded optical absorption spectra of the intermediate and Fe-rich samples reveal, apart from the UV-edge absorption, three prominent bands with maxima at ~5200, ~9500, and ~14 500 cm^{-1}. In spectra of the Fe-poor samples, the two latter bands become less conspicuous and in the most iron-poor samples they are of extremely low intensity (Fig. 4a). Observed parameters (energy, net linear extinction coefficient, and half-band widths) of these three bands as obtained through spectrum deconvolution (Fig. 4b) are summarized in Table 4. Presented uncertainties in band-intensity data are mainly related to the restricted precision of the absorber thickness measurements (±1 μm). This thickness-related error becomes disturbingly high (~10%) for data obtained from the spectra of our most Fe-rich samples, for which acceptable transmission in the NIR region could be achieved only by using very thin absorbers.

Additional weak absorption bands previously assigned to spin-forbidden $^{IV}Fe^{2+}$ or Fe^{3+} transitions (Slack 1964; Gaffney 1973; Dickson and Smith 1976) are also clearly observed in spectra of the most Fe-poor samples, but on increasing Fe content these bands become less well resolved due to a strong overlap with the intense and broad absorption band at ~14 500 cm^{-1}. A UV-edge absorption, which is probably caused by O^{2-}–Fe^{3+} and O^{2-}–Fe^{2+} charge-transfer transitions, increases strongly with the ferric concentration of the samples. The UV edge moves at increasing Fe contents and particular Fe^{3+} contents further into the visible spectral range and causes strong absorption of the blue component of the visible light. The strong Fe^{3+} influence on the UV-absorption edge is clearly illustrated by the spectra of the four samples close to end-member hercynite with variable ferric concentrations (Fig. 4c).

The absorption band at ~5200 cm^{-1} displays a considerably smaller bandwidth ($\omega_{1/2}$ ~2000 cm^{-1}) than the two major bands at higher energies ($\omega_{1/2}$ in the range 4300–6900 cm^{-1}). This indicates that these features may originate from different electronic processes. In addition, the net linear extinction coefficients (α values) of the recorded absorption bands evolve on increasing sample Fe content in highly contrasting ways. The α values of the absorption band at ~5200 cm^{-1} increase linearly with increasing Fe content, while the net intensity of the two broad bands at ~9500 and ~14 500 cm^{-1} increase in a parabolic way with increasing Fe content. The intensification of these bands as a result of increasing ferric concentration is clearly illustrated by the spectra of the four samples He100c, $He100c_{rim}$, He100e, and He100g, in which the Fe^{2+} concentration remains virtually constant but the ferric amounts differ strongly (Fig. 4c; Table 1).

The large widths displayed by the absorption bands at ~9500 and ~14 500 cm^{-1} as well as their nonlinear dependence on sample Fe content strongly indicate that they are caused by cooperative electronic processes in contrast to the band at ~5200 cm^{-1}, which shows a width in agreement with an electronic single-ion *d–d* transition origin (e.g., Mattson and Rossman 1987a).

Discussion

Fe^{2+} and Fe^{3+} ordering

Intracrystalline distribution of Fe^{2+} and Fe^{3+} in spinels is directly influenced by thermal history and chemical

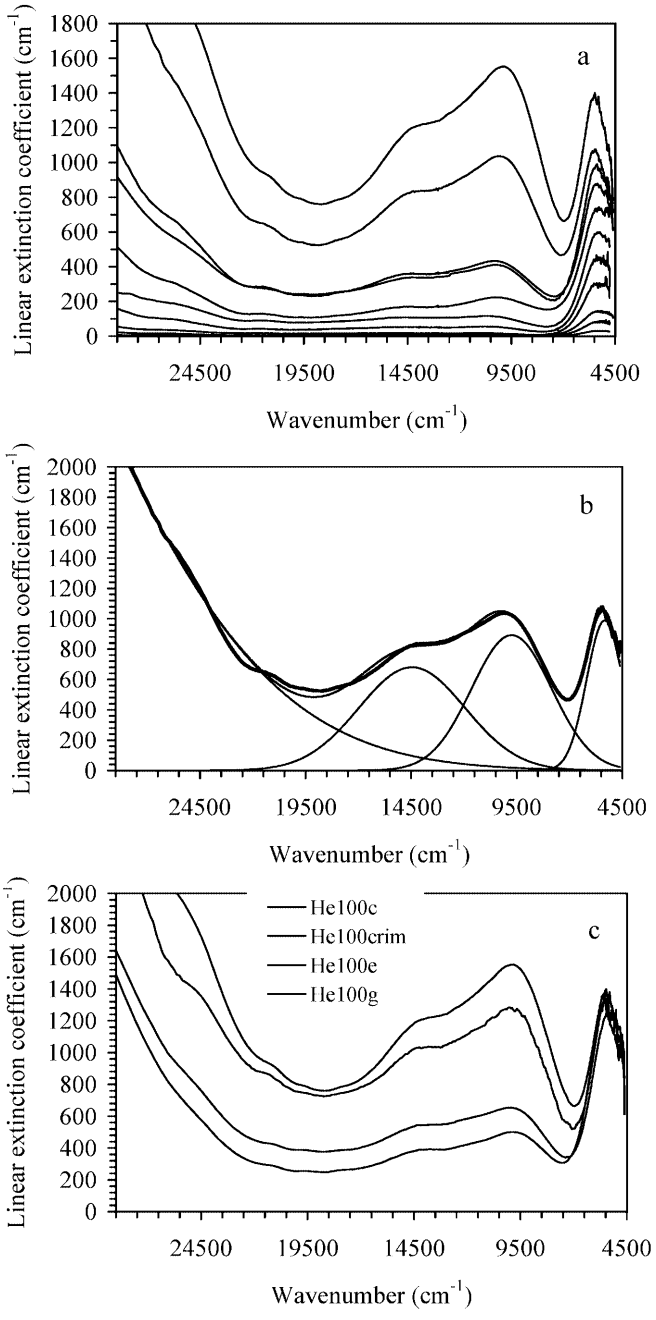

Fig. 4a–c Single-crystal optical absorption spectra of synthetic samples of the spinel *s.s.*–hercynite solid solution. **a** Optical spectra of the samples shown in decreasing order of Fe content: spectrum of He100c *at the top* and of He2d *at the bottom*. **b** Typical band fit of the present spectra illustrated by the results for the spectrum of sample He9a. **c** Optical spectra of four He100 samples showing the effects of variations in Fe^{3+} concentration

composition. All the present crystals experienced a similar thermal history and, considering that slow cooling was adopted for crystal growth between 1200 and 900 °C, and that fast kinetics of cation rearrangement has been observed in spinels above 800 °C (Andreozzi and Princivalle 2002), the estimated closure temperature is about 800 °C. This estimation is further supported by the fact that inversion values observed in samples close to spinel *s.s.* and hercynite (He2d and He100c, Table 2) are in good agreement with literature data on end members annealed at 800 °C (Larsson et al. 1994; Harrison et al. 1998; Andreozzi et al. 2000).

The influence of chemical composition is the clue to the experimentally observed variations in inversion in our samples (Table 2). The Fe^{2+} distribution as determined by XRD and Mössbauer techniques is in good agreement with calculated distributions (Andreozzi and Lucchesi 2002) applying the O'Neill and Navrotsky (1984) thermodynamic model (Fig. 5a and b) for the spinel *s.s.*–hercynite solid solution at 800 °C. Mössbauer and structure refinement results show that Fe^{2+} is progressively ordered to the T site with decreasing hercynite component (Tables 2, 3). This behavior explains why natural spinels, which usually belong to the hercynite-poor part of the join, show very low amounts of octahedrally coordinated Fe^{2+} (Andreozzi and Lucchesi 2002).

The distribution of Fe^{3+} is more difficult to constrain, due to the low amounts here observed and the strong overlap with the much more intense Fe^{2+} doublets in MS spectra. Structural data of the present samples (Andreozzi and Lucchesi 2002) indicate that an average of 77% of the total Fe^{3+} is located at the octahedral site (Table 2), and this is in agreement with previous studies on spinel *s.s.*–hercynite join, which suggested that most or all Fe^{3+} is octahedrally coordinated (Carbonin et al. 1996). Due to the mentioned difficulties, not only site assignment but even the total amount of Fe^{3+} needed careful investigation. We obtained direct measurements of Fe^{3+}/Fe_{tot} ratios by MS (Table 3), as well as structurally constrained values of Fe^{3+} concentrations through combined XRD and EMP data (Table 2), and also from EMP analyses by applying stoichiometric and charge balance constraints (Table 1). There is an overall agreement between the results (Fig. 5c), which suggest that the Fe^{3+}_{tot} content increases almost regularly along the join from about zero up to 0.07–0.10 apfu (Fig. 5c). However, whether the maximum value from MS (0.07 apfu) is slightly underestimated or, conversely, the crystal chemically inferred value (0.10 apfu) is slightly overestimated, is not straightforward. The small but systematic difference observed could be due to systematic errors in concentrations of Fe^{3+} calculated from microprobe analysis (coming from the sum of errors in all the measured elements), or small differences in sample material. As stated previously, the MS absorbers contained bulk crystal samples, whereas a few homogeneous and well-shaped crystals were selected for the XRD and OAS studies. Actually, in one case (sample He100c) a core-rim zoned sample was analyzed, and the rim region showed a lower Fe^{3+} concentration. Another possible reason for the observed systematic difference could be different recoil-free fractions for Fe^{3+} and Fe^{2+}. However, the Fe^{3+}/Fe_{tot} ratios obtained by MS on the same samples at room and low temperature were comparable, which suggests insignificant or very small differences in

recoil-free fractions for Fe^{3+} and Fe^{2+} at low temperatures.

Optical absorption band assignment

The absorption band at ~5200 cm^{-1} observed in spectra of the present spinel-group crystals is assigned, in agreement with previous studies, to a spin-allowed *d–d* transition in $^{IV}Fe^{2+}$. The peak energy recorded in the present spectra for this transition represents the high-energy component of the set of $^{IV}Fe^{2+}$ bands resulting from dynamical Jahn–Teller splitting and phonon-coupling (e.g., Slack et al. 1966; Taran and Langer 2001; Rossman and Taran 2001). An unpolarized FTIR spectrum of our sample He2*d* confirms these previous observations of a split $^5E \rightarrow {}^5T_2$ transition in $^{IV}Fe^{2+}$. The excellent linear correlation of the extinction coefficient of the 5200 cm^{-1} band with sample $^{IV}Fe^{2+}$ concentration further corroborates our band assignment (Fig. 6). Our data suggest that the molar extinction coefficient for the unresolved NIR band due to the spin-allowed $^5E \rightarrow {}^5T_2$ transition in $^{IV}Fe^{2+}$ in spinel *s.s.*–hercynite solid solution minerals is 59 ± 4 l mol^{-1} cm^{-1} (R^2 = 0.98).

In addition to the $^{IV}Fe^{2+}$ band, we observe in the present spinel spectra an absorption band (~9500 cm^{-1}, v_2 of Table 4) at energies comparable to the one recorded for the band assigned to $^{VI}Fe^{2+}$ in spinel (Mao and Bell 1975; Dickson and Smith 1976). However, the net linear extinction coefficient (α_{net}) of this band as recorded in our spectra is nonlinearly related to the $^{VI}Fe^{2+}$ concentration of the samples. This behavior contradicts a single-ion *d–d* transition origin, but supports an assignment to a process involving ferrous as well as ferric iron. Furthermore, the resulting molar extinction coefficient (ε) of this band, assuming a single-ion $^{VI}Fe^{2+}$ origin, varies in our spectra between 100 and 400 l mol^{-1} cm^{-1}. This is in strong contrast to a calculated ε value of ~0.5 l mol^{-1} cm^{-1} for the band assigned by Dickson and Smith (1976) to the single-ion $^5T_{2g} \rightarrow {}^5E_g$ transition in $^{VI}Fe^{2+}$. At higher energies (~14 500 cm^{-1}), an additional prominent absorption band (v_1 in Table 4) is recorded. The α values of this band are also nonlinearly related to the Fe^{2+} concentration of the samples, and the width of the band is much larger than generally observed for bands caused by electronic transitions in single 3*d* cations. Also in this case processes involving ferrous as well as ferric iron must be considered as potential origins.

The structural array in the spinel structure (where M sites share edges with other M sites and corners with T sites, but these latter are isolated from each other) restricts possible occurrences of electronic IVCT and ECP processes to heterovalent cations in M–M or T–M clusters. Possible heterovalent pair constellations are consequently $^{VI}Fe^{2+}$–$^{VI}Fe^{3+}$, $^{IV}Fe^{2+}$–$^{VI}Fe^{3+}$, and $^{VI}Fe^{2+}$–$^{IV}Fe^{3+}$. From the results of structural refinements (Table 2), it is evident that the $^{IV}Fe^{3+}$ concentrations are very low, hence $^{VI}Fe^{2+}$–$^{IV}Fe^{3+}$ clusters are also expected to be present at extremely low amounts and consequently only very minor contributions from electronic processes in such clusters are expected. In addition, the results of Mattson and Rossman (1987a) strongly suggest that Fe^{2+}–Fe^{3+} IVCT processes in oxygen-based structures are restricted to clusters of cations located in edge- or face-sharing sites. As a consequence, only electronic charge transfer between neighboring $^{VI}Fe^{2+}$–$^{VI}Fe^{3+}$ ions are expected to give rise to IVCT bands in spectra of ferric-containing spinel-hercynite solid-solution crystals. The absorption band at ~14 500 cm^{-1} displays all the characteristic features (band width, α value, and energy) observed for absorption bands due to Fe^{2+}–Fe^{3+} IVCT processes in oxygen-based minerals (Mattson and Rossman 1987a). Furthermore, it occurs at energies higher than those of the spin-allowed $^{VI}Fe^{2+}$ and $^{IV}Fe^{2+}$ transitions in spinel minerals, and the α value of this band displays an excellent linear correlation ($R^2 = 0.97$) with the $[^{VI}Fe^{2+}]\cdot[^{VI}Fe^{3+}]$ concentration product of the present samples (Fig. 7a), when we assume $[^{VI}Fe^{3+}]$ to constitute 77% of the total Fe^{3+}, as suggested by crystal-structural data (Andreozzi and Lucchesi 2002). Taking these features into consideration, we propose that the absorption band at ~14 500 cm^{-1} in Fe^{3+}-bearing spinel–hercynite solid solution crystals are caused by an IVCT process in $^{VI}Fe^{2+}$–$^{VI}Fe^{3+}$ clusters. On increasing Fe content, a slight decrease in peak energy is observed

Table 4 Optical absorption band parameters of synthetic crystals of the spinel *s.s.*–hercynite solid solution v = absorption band position; α = net linear extinction coefficient; ω = band width at half height

Sample	Thickness (μm)	v_1 (cm^{-1})	α_1 (cm^{-1})	ω_1 (cm^{-1})	v_2 (cm^{-1})	α_2 (cm^{-1})	ω_2 (cm^{-1})	v_3 (cm^{-1})	α_3 (cm^{-1})	ω_3 (cm^{-1})
He2d	170	14 750	0.4	6303	10 670	0.6	4709	5215	32	2034
He2f	245	14 870	1.2	6523	10 600	1.6	4451	5191	84	1973
He3a	116	14 940	7	6499	10 313	8	5001	5207	144	2035
He4b	20	14 860	43	6223	10 027	39	4625	5228	450	1933
He5a	19	14 900	82	6250	10 115	86	4796	5224	595	1960
He6a	25	14 902	131	6358	9662	189	5073	5153	719	2204
He7a	16	14 760	281	6216	9855	355	4853	5255	845	2034
He8a	14	14 507	259	6828	9803	307	4559	5304	952	1971
He9a	14	14 630	687	6005	9791	892	4678	5327	985	1980
He100c	11	14 340	921	5746	9576	1271	4352	5357	1237	1822
$He100c_{rim}$	11	14 220	705	5887	9695	1013	4311	5297	1256	1868
He100e	11	14 375	401	6122	9691	522	4539	5317	1155	1955
He100g	15	14 340	311	6124	9573	417	4428	5398	1268	1987

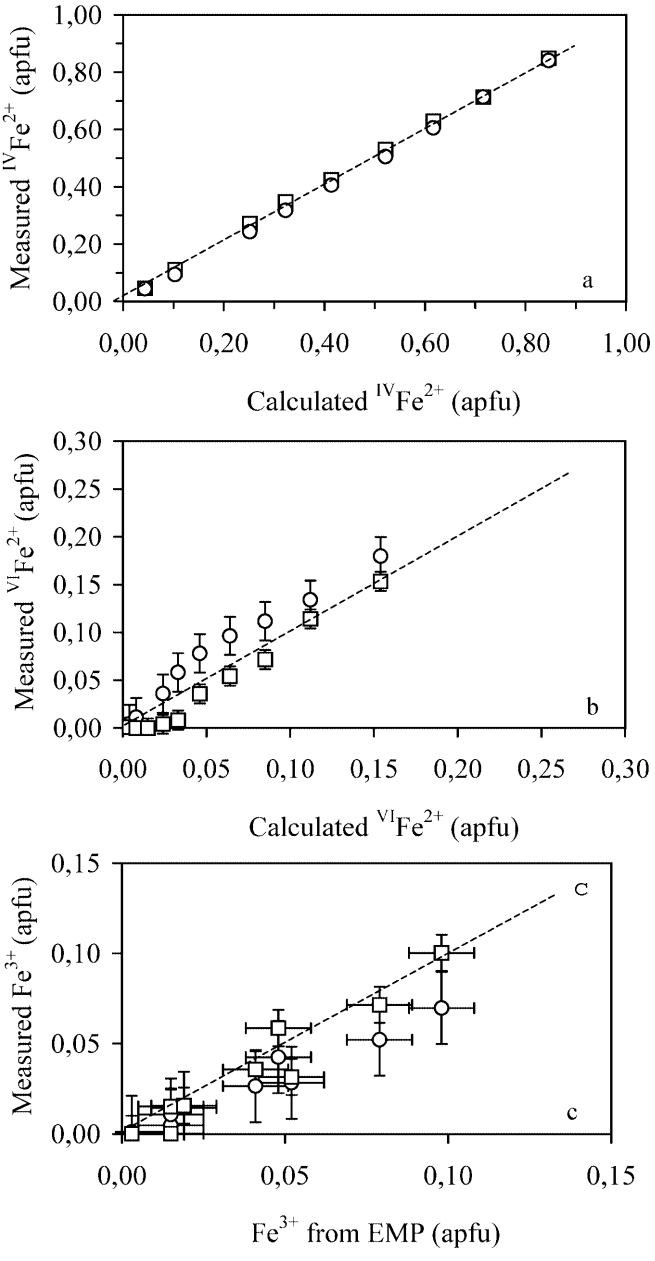

Fig. 5a–c Comparison between measured and calculated Fe concentrations in synthetic spinel *s.s.*–hercynite solid solution samples. In all diagrams: *open circles* data from MS, with contents in apfu obtained on basis of total Fe measured by EMP; *open squares* data from combined structure refinement and EMP analyses; *dashed line* 1:1 relation; *error bars* correspond to $\pm 2\sigma$. **a** Measured $^{IV}Fe^{2+}$ contents with respect to the same quantities calculated by using the thermodynamic model for spinel solid solutions (O'Neill and Navrotsky 1984). **b** Measured $^{VI}Fe^{2+}$ contents with respect to the same quantities calculated by using the O'Neill and Navrotsky model. **c** Measured Fe^{3+} contents with respect to the same quantities retrieved by EMP analyses assuming ideal stoichiometry (three cations per four anions)

for this broad band (Table 4), which may be attributed to an increasing contribution from electron transfers within larger clusters of $^{VI}Fe^{2+}$ and $^{VI}Fe^{3+}$. This effect would be in agreement with a proposed lowering of energies of IVCT processes with increasing degree of polymerization of the metal-centered sites in oxygen-based minerals (Amthauer and Rossman 1984).

Electronic transitions in exchange-coupled pairs have been recorded to contribute to the spectra of minerals, in which the participating cations are located at sites that share faces, edges, or just corners (e.g., Smith 1978; Smith et al. 1983; Andreozzi et al. 2001b). This indicates that spectra of spinels characterized by the present Fe intersite distribution may display ECP bands due to electronic transitions in $^{VI}Fe^{2+}$–$^{VI}Fe^{3+}$ as well as in $^{IV}Fe^{2+}$–$^{VI}Fe^{3+}$ pairs. As ECP bands are supposed to occur at energies comparable or identical to those of electronic *d–d* transitions in the participating single ions (Smith 1978), such pair bands should be located at or close to 10 000 cm^{-1} (spin-allowed *d–d* transition in single-ion $^{VI}Fe^{2+}$) and 5000 cm^{-1} (spin-allowed *d–d* transition in single-ion $^{IV}Fe^{2+}$) in our spectra. As mentioned above, we do observe in our spectra intense absorption bands at ~9500, which is very close in energy to the spin-allowed $^5T_{2g} \rightarrow {}^5E_g$ transition in $^{VI}Fe^{2+}$ in spectra of spinel *s.s.*–hercynite solid-solution minerals (Mao and Bell 1975; Dickson and Smith 1976). However, the α value of this band is very poorly correlated with the Fe^{2+} concentration of the samples, which indicates a different origin for this feature. In fact, the net linear extinction coefficient of this absorption band shows very good correlations ($R^2 = 0.98$) with the $[Fe^{2+}_{tot}] \cdot [Fe^{3+}_{tot}]$ sample concentration product. Furthermore, a comparably good correlation is also observed for both products $[^{VI}Fe^{2+}]\cdot[^{VI}Fe^{3+}]$ and $[^{IV}Fe^{2+}]\cdot[^{IV}Fe^{3+}]$. However, based on the fact that this band occurs at energies lower than are generally observed for Fe^{2+}–Fe^{3+} IVCT bands but close to that of the $^5T_{2g} \rightarrow {}^5E_g$ transition in $^{VI}Fe^{2+}$ in spinel, in combination with the very good linear correlation ($R^2 = 0.98$) between net linear extinction of the band and the concentration of $^{VI}Fe^{2+}$–$^{VI}Fe^{3+}$ pairs in the samples (Fig. 7b), we assign this band to a transition in exchange-coupled Fe^{2+}–Fe^{3+} pairs at octahedral sites in the spinel structure. The energy of this band decreases slightly with increasing Fe content (Table 4), which may be ascribed to increasing ^{VI}Fe–O bond lengths and resulting decrease in splitting between the $2t_g$ and e_g 3*d* orbital levels in ^{VI}Fe. Contributions from single ion $^5T_{2g} \rightarrow {}^5E_g$ transition in $^{VI}Fe^{2+}$ to the spectra of our samples cannot be excluded, but considering the low ε values (~0.5 l mol^{-1} cm^{-1}) for this transition (Dickson and Smith 1976) in combination with the very high intensity of the overlapping ECP band, it is concluded that such contributions are highly subordinate and amount in the present spectra to less than 0.5% of the absorption in this energy region.

Potential applications

It is here suggested that the correlation constants presented above may be utilized to rapidly estimate the Fe

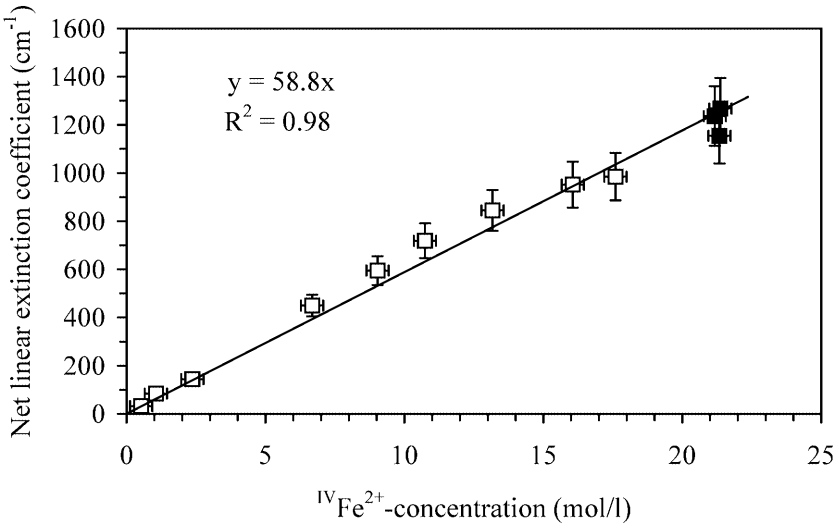

Fig. 6 Correlation plot of the net linear extinction coefficient of the absorption band at ~5200 cm^{-1} as a function of the concentration of ferrous iron in tetrahedral coordination. *Black squares* represent the three samples He100c, He100e, and He100g; the *solid line* is a linear regression of the data set; *error bars* correspond to $\pm 1\sigma$

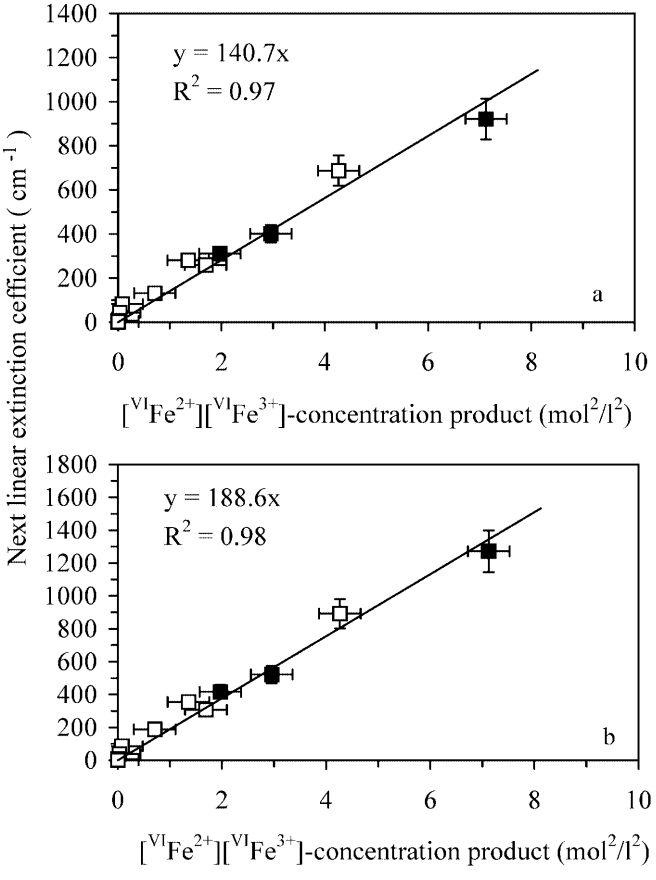

Fig. 7a,b Correlation plots of net linear extinction coefficients of the absorption bands at ~14 500 cm^{-1} (**a**) and at ~9500 cm^{-1} (**b**) as a function of the concentration product of ferrous and ferric iron in octahedral coordination. *Black squares* represent the three samples He100c, He100e, and He100g; the *solid line* shows a linear regression fit of the data set; *error bars* correspond to $\pm 1\sigma$

distribution in microchemically analyzed spinel crystals from optical absorption spectra. By applying optical microscope spectrometry, such estimates may in principle be obtained from small crystals or discrete areas of zoned crystals directly in petrographic thin sections with a spatial resolution of approximately 10 μm. As an illustration of this application, we may use the spectrum of a thin rim ($He100c_{rim}$) of an additional synthetic crystal (Fig. 4c). In contrast to all of the previously discussed spectra, which constitute the basis for the derived band correlation constants, this additional one was recorded with a smaller measure aperture diameter of 20 μm. The total Fe concentration in the rim of this crystal corresponds to 44.1 wt% FeO, (Table 1) which equals 27.0 mol Fe l^{-1}. From the optical spectrum of the sample and specifically the net linear absorption coefficient (α_{net}) of the band at ~5200 cm^{-1} (Table 4) a ^{IV}Fe concentration of 21.3 mol l^{-1} is indicated. The α_{net} values of the absorption bands at ~14 500 and ~9500 cm^{-1} recorded in the spectrum of $He100c_{rim}$ (Table 4) suggest that the $[^{VI}Fe^{2+}]\cdot[^{VI}Fe^{3+}]$ concentration product in the rim of this crystal equals 5.0–5.4 mol^2 l^{-2}. Provided that ~75% of the ferric iron is located at octahedral sites in Mg–Fe–Al spinels, which is indicated by the spinel structural refinements of Andreozzi and Lucchesi (2002), an $^{VI}Fe^{3+}$ concentration of 1.3–1.4 mol l^{-1} and an $^{VI}Fe^{2+}$ concentration of 3.8–4.0 mol l^{-1}, or vice versa, is calculated. From the overall chemistry of the rim in combination with charge balance considerations (Table 1), it is obvious that the lower value for $[^{VI}Fe^{3+}]$ represents the real solution to the equation. Due to the small size of this crystal rim we cannot offer any XRD refinement or Mössbauer data to validate these figures. However, as a crude test we may compare the Fe^{3+} concentration as determined from the optical spectra with the Fe^{3+} concentration calculated directly from the electron microprobe analyses of the rim. At a $[^{VI}Fe^{3+}]/[^{IV}Fe^{3+}]$ distribution ratio of 3:1 an $^{VI}Fe^{3+}$ concentration of 1.3–1.4 mol l^{-1} is calculated from the optical data. This corresponds to a total Fe^{3+} concentration of 1.7–1.9 mol l^{-1} or 3.1–3.4 wt% Fe_2O_3, which is in very good agreement with the value of 3.4 wt% Fe_2O_3 calculated directly from the EMP data of the rim.

Conclusions

Results obtained on a series of single crystals on the spinel *s.s.*–hercynite join indicate that Fe^{2+} ordering may be assessed by monitoring the net linear extinction coefficient of an absorption band at ~5200 cm^{-1}, which is linearly proportional to the $^{IV}Fe^{2+}$ concentration. The molar extinction coefficient, ε, for this band is determined to be 59 ± 4 l mol^{-1} cm^{-1}. Consequently, OAS measurements may provide data necessary to determine cation distribution in members of the binary solid solution, provided that accurate EMP analyses are available.

Crystals containing ferric iron show more complex spectra. This is explained on the basis of electronic $^{VI}Fe^{2+}$–$^{VI}Fe^{3+}$ IVCT and $^{VI}Fe^{2+}$–$^{VI}Fe^{3+}$ ECP transitions, which give rise to broad and very intense absorption bands in the NIR spectra at ~14 500 and ~9500 cm^{-1}, respectively. The net linear extinction coefficients of these bands increase as a function of the sample $[^{VI}Fe^{2+}]\cdot[^{VI}Fe^{3+}]$ concentration product. This provides the possibility to determine the ferric concentration through measurements of the net linear extinction coefficients of the prominent absorption bands at ~9500 and ~14 500 cm^{-1}. The α values of these two bands are linearly dependent on the concentrations and ordering of ferrous and ferric iron, as:

$$\alpha_{9500} = 189 \pm 36\ [^{VI}Fe^{2+}] \cdot [^{VI}Fe^{3+}] \quad \text{and}$$

$$\alpha_{14500} = 141 \pm 25\ [^{VI}Fe^{2+}] \cdot [^{VI}Fe^{3+}]\ ,$$

where concentrations are expressed in mol l^{-1}.

Mineralogical applications of the OAS technique benefit from a high spatial resolution, which allows in situ studies on areas as small as 10 μm in diameter. Consequently, OAS may be used as a "microprobe" for Fe^{2+} and Fe^{3+} intracrystalline distribution in small crystals or samples showing zonation in composition and/or ordering. Furthermore, it must be noticed that mixed valence Fe^{2+}–Fe^{3+}-bearing spinels show completely different spectra from either pure Fe^{2+} or Fe^{3+} spinels (see also Andreozzi et al. 2001b). The color of our Fe^{3+}-bearing spinel *s.s.*–hercynite crystals is highly sensitive to small variations in the ferric amount. In addition to the bands at ~9500 and ~14 500 cm^{-1}, the absorption of blue light strongly increases with increasing ferric concentrations due to intense ligand-metal charge transfer processes. This explains why crystals with low concentration products $[^{VI}Fe^{2+}]\cdot[^{VI}Fe^{3+}]$ are blue to violet in color, while they become green, grading almost to black, in thick sections at increasing concentrations of both $^{VI}Fe^{2+}$ and $^{VI}Fe^{3+}$.

Acknowledgements We thank Dr. Udawatte for discussions about spinel synthesis, Prof. Lucchesi (University of Rome La Sapienza) for sharing unpublished structural data, and Mr. Carampin (CNR, Padova) for technical assistance during electron microprobe analysis. This manuscript benefited from detailed and constructive comments of an anonymous reviewer. We gratefully acknowledge support from the Swedish Research Council (VR) and the Italian Research Council (CNR).

References

Amthauer G, Rossman GR (1984) Mixed valence of iron in minerals with cation clusters. Phys Chem Miner 11: 37–51

Andreozzi GB, Lucchesi S (2002) Intersite distribution of Fe^{2+} and Mg in the spinel *s.s.*–hercynite series by single-crystal X-ray diffraction. Am Mineral (in press)

Andreozzi GB, Princivalle F (2002) Kinetics of cation ordering in synthetic $MgAl_2O_4$ spinel. Am Mineral (in press)

Andreozzi GB, Princivalle F, Skogby H, Della Giusta A (2000) Cation ordering and structural variations with temperature in $MgAl_2O_4$ spinel: an X-ray single-crystal study. Am Mineral 85: 1164–1171

Andreozzi GB, Bosi F, Garramone F (2001a) Synthetic spinels in the (Mg, Fe^{2+}, Zn) (Al, Fe^{3+})$_2O_4$ system. II. Preliminary chemical and structural data of hercynite and magnesioferrite samples. Period Mineral 70: 193–204

Andreozzi GB, Hålenius U, Skogby H (2001b) Spectroscopic active $^{IV}Fe^{3+}$–$^{VI}Fe^{3+}$ clusters in spinel-magnesioferrite solid-solution crystals: a potential monitor for ordering in oxide spinels. Phys Chem Miner 28: 435–444

Andreozzi GB, Lucchesi S, Skogby H, Della Giusta A (2001c) Compositional dependence of cation distribution in some synthetic (Mg,Zn)(Al,Fe^{3+})$_2O_4$ spinels. Eur J Mineral 13: 391–402

Bohlen SR, Dollase WA, Wall VJ (1986) Calibration and applications of spinel equilibria in the system FeO–Al_2O_3–SiO_2. J Petrol 27: 1143–1156

Burns RG (1993) Mineralogical applications of crystal field theory, 2nd ed. In: Putnis A, Lieberman RC (eds), Cambridge topics in mineral physics and chemistry 5, Cambridge University Press, Cambridge

Carbonin S, Russo U, Della Giusta A (1996) Cation distribution in some natural spinels from X-ray diffraction and Mössbauer spectroscopy. Mineral Mag 60: 355–368

Cremer V (1969) Die Mischkristallbildung im System Chromit–Magnetit–Hercynit zwischen 1000 und 500 °C. N Jahrb Mineral Abh 111: 184–205

Della Giusta A, Carbonin S, Ottonello G (1996) Temperature-dependent disorder in a natural Mg–Al–Fe^{2+}–Fe^{3+} spinel. Mineral Mag 60: 603–616

Dickson BL, Smith G (1976) Low-temperature optical absorption and Mössbauer spectra of staurolite and spinel. Can Mineral 14: 206–215

Frost BR, Shive PN (1986) Magnetic mineralogy of the lower continental crust. J Geophys Res 91: 6513–6521

Gaffney ES (1973) Spectra of tetrahedral Fe^{2+} in $MgAl_2O_4$. Phys Rev (B) 8: 3484–3486

Hafner S (1960) Metalloxyde mit Spinellstruktur. Schweiz Mineral Petrol Mitt 40: 208–240

Haggerty SE (1978) Mineralogical constraints on Curie isotherms in deep crustal magnetic anomalies. Geophys Res Lett 5: 105–108

Harrison RJ, Redfern SAT, O'Neill HStC (1998) The temperature dependence of the cation distribution in synthetic hercynite ($FeAl_2O_4$) from in-situ neutron diffraction refinements. Am Mineral 83: 1092–1099

Hill RJ (1984) X-ray powder diffraction profile refinement of synthetic hercynite. Am Mineral 69: 937–942

Hill RJ, Craig JR, Gibbs GV (1979) Systematics of the spinel structure type. Phys Chem Miner 4: 317–340

Jernberg P, Sundqvist T (1983) A versatile Mössbauer analysis program. Uppsala University, Institute of Physics (UUIP-1090)

Kristiansson P, Hålenius U, Skogby H, Elfman M, Malmqvist K, Pallon J (1999) Boron distribution in single crystals investigated by nuclear reaction analysis. Nucl Instr Meth Phys Res (B) 158: 562–567

Larsson L (1994) Temperature dependence of the intra-crystalline distribution in some iron-containing spinels. PhD Thesis, Acta Universitatis Upsaliensis, Uppsala 1994

Larsson L (1995) Temperature-dependent cation distribution in a natural $Mg_{0.4}Fe_{0.6}Al_2O_4$ spinel. N Jahrb Mineral Mh 173: 184

Larsson L, O'Neill HStC, Annersten H (1994) Crystal chemistry of synthetic hercynite ($FeAl_2O_4$) from XRD structural refinements and Mössbauer spectroscopy. Eur J Mineral 6: 39–51

Lehmann J, Roux J (1986) Experimental and theoretical study of $(Fe^{2+},Mg)(Al,Fe^{3+})_2O_4$ spinels: activity–composition relationships, miscibility gaps, vacancy contents. Geochim Cosmochim Acta 50:1765–1783

Lucchesi S, Della Giusta A (1997) Crystal chemistry of a highly disordered Mg–Al natural spinel. Mineral Petrol 59: 91–99

Lucchesi S, Amoriello M, Della Giusta A (1998a) Crystal chemistry of spinels from xenoliths of the Alban Hills volcanic region. Eur J Mineral 10: 473–482

Lucchesi S, Della Giusta A, Russo U (1998b) Cation distribution in natural Zn-aluminate spinels. Mineral Mag 62: 41–54

Lucchesi S, Russo U, Della Giusta A (1999) Cation distribution in natural Zn-spinels: franklinite. Eur J Mineral 11: 501–511

Mao HK, Bell PM (1975) Crystal-field effects in spinel: oxidation states of iron and chromium. Geochim Cosmochim Acta 39: 865–874

Mattioli GS, Wood BJ (1988) Magnetite activities across the $MgAl_2O_4$–Fe_3O_4 join, with application to thermobarometric estimates of upper mantle oxygen fugacity. Contrib Mineral Petrol 98: 148–162

Mattson SM, Rossman GR (1987a) Identifying characteristics of charge transfer transitions in minerals. Phys Chem Miner 14: 94–99

Mattson SM, Rossman GR (1987b) Fe^{2+}–Fe^{3+} interactions in tourmaline. Phys Chem Miner 14: 163–171

Okaj T, Wada H, Fujinuki T (1996) Ignition and chemical resistance tests of platinum and platinum-alloy crucibles for chemical analysis (in Japanese with English abstract). Bunseki-Kagaku 45: 1127–1132

O'Neill HStC, Navrotsky A (1984) Cation distribution and thermodynamic properties of binary spinel solid solutions. Am Mineral 69: 733–753

O'Neill HStC, Wall VJ (1987) The olivine-spinel oxygen geobarometer, the nickel precipitation curve and the oxygen fugacity of the upper mantle. J Petrol 28: 1169–1192

O'Neill HStC, Dollase WA (1994) Crystal structures and cation distributions in simple spinels from powder XRD structural refinements: $MgCr_2O_4$, $ZnCr_2O_4$, Fe_3O_4 and the temperature dependence of the cation distribution in $ZnAl_2O_4$. Phys Chem Miner 20: 541–555

O'Neill HStC, Annersten H, Virgo D (1992) The temperature dependence of the cation distribution in magnesioferrite ($MgFe_2O_4$) from powder XRD structural refinements and Mössbauer spectroscopy. Am Mineral 77: 725–740

Pouchou JL, Pichoir F (1984) A new model for quantitative X-ray microanalysis. I. Application to the analysis of homogeneous samples. Rech Aérospat 3: 13–36

Princivalle F, Della Giusta A, De Min A, Piccirillo EM (1999) Crystal chemistry and significance of cation ordering in Mg–Al-rich spinels from high-grade hornfels (Predazzo-Monzoni, NE Italy). Mineral Mag 63: 257–262

Redfern SAT, Harrison RJ, O'Neill HStC, Wood DRR (1999) Thermodynamics and kinetics of cation ordering in $MgAl_2O_4$ spinel up to 1600 °C from in situ neutron diffraction. Am Mineral 84: 299–310

Rossman GR, Taran MN (2001) Spectroscopic standards for four- and fivefold-coordinated Fe^{2+} in oxygen-based minerals. Am Mineral 86: 896–903

Slack GA (1964) $FeAl_2O_4$–$MgAl_2O_4$: growth and some thermal, optical, and magnetic properties of mixed single crystals. Phys Rev 134: (A)1268–(A)1280

Slack GA, Ham FS, Chrenko RM (1966) Optical absorption spectra of tetrahedral Fe^{2+} ($3d^6$) in cubic ZnS, CdTe and $MgAl_2O_4$. Phys Rev 152: 376–402

Smith G (1978) Evidence for absorption by exchange-coupled Fe^{2+}–Fe^{3+} pairs in the near infra-red spectra of minerals. Phys Chem Miner 3: 375–383

Smith G, Hålenius U, Annersten H, Ackermann L (1983) Optical and Mössbauer spectra of manganese-bearing phlogopites: $^{IV}Fe^{3+}$–$^{VI}Mn^{2+}$ pair absorption as the origin of reverse pleochroism. Am Mineral 68: 759–768

Taran MN, Langer K (2001) Electronic absorption spectra of Fe^{2+} in oxygen-based rock-forming minerals at temperatures between 297 and 600 K. Phys Chem Miner 28: 199–210

Turnock A, Eugster HP (1962) Fe–Al oxides: phase relationships below 1000 °C. J Petrol 3: 533–565

Waerenborgh JC, Annersten H, Ericsson T, Figueiredo MO, Cabral JMP (1990) A Mössbauer study of natural gahnite spinels showing strongly temperature-dependent quadrupole splitting distributions. Eur J Mineral 2: 267–271

Waerenborgh JC, Figueiredo MO, Cabral JMP, Pereira LCJ (1994) Powder XRD structure refinements and ^{57}Fe Mossbauer effect study of synthetic $Zn_{1-x}Fe_xAl_2O_4$ ($0 < x \leq 1$) spinels annealed at different temperatures. Phys Chem Miner 21: 460–468